A parallel domain decomposition method for large eddy simulation of blood flow in human artery with resistive boundary condition

Zi-Ju Liao [a], Shanlin Qin [b], Rongliang Chen [b], Xiao-Chuan Cai [c],*

[a] Department of Mathematics, College of Information Science and Technology, Jinan University, Guangzhou 510632, China
[b] Shenzhen Institutes of Advanced Technology, Chinese Academy of Sciences, Shenzhen 518055, China
[c] Department of Mathematics, University of Macau, Macau, China

ARTICLE INFO

ABSTRACT

In this paper, we present a parallel domain decomposition algorithm for the simulation of blood flows in patient-specific artery. The flow may be turbulent in certain situations such as when there is stenosis or aneurysm. An accurate simulation of the turbulent effect is important for the understanding of the hemodynamics. Direct numerical simulation is computationally expensive in practical applications. As a result, most researchers choose to focus on a portion of the artery or use a low-dimensional approximation of the artery. In this paper, we focus on the large eddy simulation (LES) of blood flows in the abdominal aorta. To make the model more physiologically accurate, we consider a resistive outflow boundary condition which is more accurate than the traditional traction free condition. Different from the common decoupled approach where the resistive boundary condition is pre-calculated and then imposed as a Neumann condition, we prescribe it implicitly as an integral term on the LES equations and solve the coupled system monolithically. The governing system of equations is discretized by a stabilized finite element method in space and an implicit second-order backward differentiation scheme in time. A parallel Newton–Krylov–Schwarz algorithm is applied for solving the resulting nonlinear system with analytic Jacobian. Due to the integral nature of the resistive boundary condition, the Jacobian matrix has a dense block corresponding to all the variables on the outlet boundaries. Impacts of the resistive boundary condition with different parameters on the simulation results and the performance of the algorithm are investigated in detail. Numerical experiments show that the algorithm is stable with large time step size and is robust with respect to other parameters of the solution algorithm. We also report the parallel scalability of the algorithm on a supercomputer with over one thousand processor cores.

1. Introduction

With the rapid development of computing technology, computational fluid dynamics (CFD) is becoming an powerful tool for understanding the hemodynamics of certain vascular diseases and thereby improve the diagnosis and treatment. For example, CFD has been employed to study the hemodynamics of aortic and cerebral aneurysms [1, 2], the diagnosis of coronary artery disease [3,4], and to understand the hemodynamic effect of the endovascular treatment [5–7]. The advantages of the CFD approach lie in that it is low-cost and non-invasive, and it can obtain some important physical quantities that are immeasurable directly, such as the dynamic value of wall shear stress [8] which has been shown highly correlated to some vascular diseases like the aortic aneurysm formation and growth [9,10]. However, there are still several challenging problems to be addressed when applying CFD to realistic human vascular simulations. The difficulties

come from the complex geometry with multiple branches, the definition of physiologically correct inflow/outflow boundary conditions, and the modeling of the turbulent and transitional flows, etc. Moreover, in order to apply the computational technology for clinical applications, the large-scale calculation should be carried out in a reasonable amount of time. Due to the limited parallelism, most of the published works focus on the study of steady-state problems or problems defined on a small portion of an artery tree. In the scalable approach to be introduced in this paper, the computing time can be reduced when the number of processors is increased even when the artery tree is large and complex.

Similar to other fluid mechanics applications, special attention would need to be given on the boundary conditions (BC) which play a major role in determining the simulation results. At the inlet, the time-varying inflow rate from direct clinical measurement is prescribed as

a Dirichlet boundary condition with different velocity profiles such as the blunt profile, the parabolic profile, the Womersley profile, or the measured patient-specific velocity profiles when available [11–15]. The effect of inlet velocity profiles on the simulation results has been investigated, and the conclusions seem to be problem dependent. In [11,12], it was found that the selection of inlet velocity conditions significantly affects only the flow region close to the inlet of the aorta. However, in [15], it recommends the use of the pulsatile parabolic profile over the blunt or Womersley profiles because it provided results most similar to the results using the patient-specific velocity profile. Compared with the inlet boundary condition, the outlet boundary condition has a much greater influence on the simulations results. Since it is often much more difficult to obtain the flow information at the outlets of a multi-branched arterial network, artificial boundary conditions have to be assigned in the outlets. The traditional traction-free boundary condition often yields incorrect pressure field and flow distribution among different outlets, due to the ignorance of the influence from the truncated downstream vascular. Several works have been developed to address this issue. For example, Grinberg and Karniadakis [16] proposed a method to incorporate the clinically measured outflow rates for the pressure boundary condition at multiple outlets. Lancellotti et al. [17] presented a SUPG stabilized $P_2 - P_2$ finite element method for the large eddy simulation of blood flows in realistic carotid artery, where they imposed a fixed flow division for the outlets and used a Lagrange multiplier to constrain the velocity profile. Bulant et al. [18] proposed a resistive boundary condition for flows in the coronary, and they presented a strategy to calculate the resistance for the multiple coronary vessels. In these approaches, the pressure and the flow rate on the outlets are measured or calculated based on the model beforehand, and then imposed as a Neumann condition on the outlet boundaries. Therefore, the evaluation of the model and the solving of the fluid equations are decoupled. The advantage of this approach is that it is easy to implement and has little or no increase in the computational cost. However, the prescription of Neumann conditions on the outlet boundaries may introduce numerical instability known as the backflow instability, especially in large vessels. Several works have been developed to deal with this problem [19–21]. A more accurate and stable approach is to couple the model for the outlet boundary into the system of equations. Vignon et al. [22,23] developed a framework of stabilized finite element method for solving the 3D incompressible Navier–Stokes equations coupled with a lumped parameter model for the outflow boundary conditions. Wu et al. [24,25] proposed a parallel finite element method which prescribed the resistance outflow boundary condition implicitly on the outlet boundaries, and solve the coupled system monolithically. Simulation results of blood flows in branching arteries validated the accuracy of the coupled approach. Because of the high computational cost, most of the published works for studying blood flows in human arteries only consider the simplified geometrical model, where the flows are also relatively simple. In this work, we consider a full 3D model of a patient-specific coronary and abdominal artery with aneurysm. For such geometrically complex artery, the fluid is unsteady turbulent with secondary structures [26], therefore, large eddy simulation (LES) approach is adopted in this study.

Since the blood flow in the human artery is usually not fully developed, highly anisotropic and non-homogeneous, the classical Smagorinsky model is not suitable to model the small eddies in such transient and turbulent flows as it is too dissipative. Instead, we apply the σ-model [27] based on the singular values of the stress tensor to model the motion of subgrid scales. A fully implicit finite element method is introduced to solve the incompressible LES equations coupled with the resistive outflow boundary condition. Specifically, on each outlet, the pressure P is assumed to be constant and the relation $P = P_{\text{ref}} + QR$ is implicitly prescribed, where P_{ref} is a reference value related to the terminal (venous) pressure, Q is the flow rate at the outlet, and R is the resistance representing the influence from absent parts of the circulation system. Usually, the values of the resistance are different in

different outlets. By assuming a total resistance R_{total}, the resistance for each outlet can be defined using the well-known Murray's law [18]. We shall investigate in detail the impact of the parameters of the resistive boundary condition on the simulation results. We discretize the governing equations by a stabilized $P_1 - P_1$ finite element method in space and an implicit second-order backward differentiation scheme in time. The discretization leads to a large system of nonlinear equations for each time step. To solve the systems, we consider a Newton–Krylov–Schwarz (NKS) algorithm. Specifically, an inexact Newton method is used to solve the nonlinear algebraic system, within which a restricted additive Schwarz preconditioned Krylov subspace method is used to solve the analytically computed Jacobian matrix. For traditional traction-free boundary condition, the Jacobian matrix is uniformly sparse and each variable is related through the function only to the neighboring variables. However, for the coupled resistive boundary condition, the Jacobian matrix is computationally more challenging since it has a dense block corresponding to all variables on the outlet boundaries due to the integral nature of the resistive boundary condition. We perform extensive numerical experiments to show the robustness and efficiency of the proposed algorithm with respect to the physical and numerical parameters. Parallel scalability of the algorithm on a supercomputer with over one thousand processor cores is also reported.

The remainder of this paper is organized as follows. In Section 2, the LES equations and the resistive boundary conditions are introduced, then the numerical method is presented, including the implicit finite element discretization and the parallel Newton–Krylov–Schwarz algorithm. In Section 3, a patient-specific case is studied. The robustness and scalability of the proposed method are also studied in this section. Some concluding remarks are given in Section 4.

2. Numerical methods

2.1. The flow model

We consider the blood flow in medium and large arteries. In this case, it is reasonable to assume the fluid is Newtonian that can be modeled by the incompressible Navier–Stokes equations [28]. In large eddy simulation, the fluid velocity $\boldsymbol{u}$ is decomposed into a filtered (resolved) part $\bar{\boldsymbol{u}}$ and the remaining unsolved part $\boldsymbol{u}'$, so that $\boldsymbol{u} = \bar{\boldsymbol{u}} + \boldsymbol{u}'$. The pressure is also decomposed similarly as $p = \bar{p} + p'$. Only the resolved quantities are computed by LES. The effect of the remaining unresolved parts are modeled. Consider a vascular domain $\Omega \in \mathbb{R}^3$ with boundary $\Gamma = \partial\Omega$, then the filtered Navier–Stokes equations for LES reads

$$\begin{cases} \dfrac{\partial \bar{\boldsymbol{u}}}{\partial t} + \bar{\boldsymbol{u}} \cdot \nabla \bar{\boldsymbol{u}} = -\dfrac{1}{\rho}\nabla \bar{p} + 2\nu \nabla \cdot \boldsymbol{S}(\bar{\boldsymbol{u}}) - \nabla \cdot \boldsymbol{\tau} & \text{in } \Omega, \\ \nabla \cdot \bar{\boldsymbol{u}} = 0 & \text{in } \Omega, \end{cases} \quad (1)$$

where ρ is the fluid density, ν is the kinematic viscosity, $\boldsymbol{S}$ is the filtered strain rate tensor defined as

$$\boldsymbol{S}(\bar{\boldsymbol{u}}) = \frac{1}{2}\left(\nabla\bar{\boldsymbol{u}} + (\nabla\bar{\boldsymbol{u}})^T\right), \quad (2)$$

and

$$\boldsymbol{\tau} = \overline{\boldsymbol{u}\boldsymbol{u}} - \bar{\boldsymbol{u}}\bar{\boldsymbol{u}} \quad (3)$$

is the so-called subgrid scale (SGS) stress tensor which accounts for the effects of the small unresolved scales on the resolved ones, and it is an unclosed term of the LES equations. Usually, the SGS stress tensor is modeled in analogy with the kinetic theory of gases by introducing a subgrid-scale viscosity ν_{sgs} and by modeling the deviatoric part of the subgrid-scale tensor as follows:

$$\boldsymbol{\tau}^d(\bar{\boldsymbol{u}}) = -2\nu_{\text{sgs}}(\bar{\boldsymbol{u}})\boldsymbol{S}(\bar{\boldsymbol{u}}), \quad (4)$$

where the tensor $\boldsymbol{\tau}^d(\bar{\boldsymbol{u}}) \equiv \boldsymbol{\tau} - \dfrac{1}{3}\sum_k \tau_{kk}\, \boldsymbol{I}$ is the deviatoric part of $\boldsymbol{\tau}$. The SGS model applied in this work is the σ-model, introduced in [27]. It

is based on the singular values $\sigma_1(\mathbf{x}, t) \geq \sigma_2(\mathbf{x}, t) \geq \sigma_3(\mathbf{x}, t)$ of $\nabla \bar{\mathbf{u}}$, and the subgrid scale viscosity is defined as follows:

$$\nu_{\text{sgs}} = C\bar{\Delta}^{-2} \frac{\sigma_3(\sigma_1 - \sigma_2)(\sigma_2 - \sigma_3)}{\sigma_1^2}, \tag{5}$$

where C is a suitable constant and $\bar{\Delta}$ is the characteristic length of the filter. In [17], it was shown that the σ-model has better performance than the dynamic and dynamic mixed Smagorinsky models for the LES of blood flows in realistic stenotic carotids, where the latters encounter numerical instabilities during the numerical simulations.

By introducing the σ-model and defining the modified filtered pressure $\bar{P} \equiv \frac{\bar{p}}{\rho} - \frac{1}{3} \sum_k \tau_{kk} \mathbf{I}$, the LES equations become

$$\begin{cases} \dfrac{\partial \bar{\mathbf{u}}}{\partial t} + \bar{\mathbf{u}} \cdot \nabla \bar{\mathbf{u}} = -\nabla \bar{P} + \nabla \cdot (2\nu_t \mathbf{S}) & \text{in } \Omega, \\ \nabla \cdot \bar{\mathbf{u}} = 0 & \text{in } \Omega, \end{cases} \tag{6}$$

where $\nu_t = \nu + \nu_{\text{sgs}}$ denotes the total viscosity of the fluid.

The initial condition is imposed as

$$\bar{\mathbf{u}}(\mathbf{x}, 0) = \mathbf{u}_0(\mathbf{x}) \quad \text{in} \quad \Omega, \tag{7}$$

where $\mathbf{u}_0(\mathbf{x})$ is the initial divergence-free velocity field. In this work, a quiescent initial condition is used.

The boundary, Γ, can be decomposed into the inlet boundary Γ_{in}, the lateral wall boundary Γ_{wall} and N_o outlets of the domain Γ_{out}^k, $k = 1, 2, \ldots, N_o$. At the inlet and wall boundaries, Dirichlet boundary condition are imposed,

$$\bar{\mathbf{u}} = \mathbf{v}_I \quad \text{on } \Gamma_{\text{in}}, \tag{8}$$

$$\bar{\mathbf{u}} = \mathbf{0} \quad \text{on } \Gamma_{\text{wall}}, \tag{9}$$

where $\mathbf{v}_I$ is the given inflow velocity profile.

At each outlet boundary, a resistive boundary condition is imposed as follows:

$$\bar{P}_{\text{out}}^k = P_{\text{ref}} + R_{\text{out}}^k Q_{\text{out}}^k \quad k = 1, 2, \ldots, N_o, \tag{10}$$

where $\bar{P}_{\text{out}}^k$ is the pressure at the kth outlet, P_{ref} is a reference value related to the terminal (venous) pressure, R_{out}^k is the resistance at the kth outlet which is used to simulate the pressure losses in the peripheral vasculature, and Q_{out}^k is the flow rate at the kth outlet, taking the form $Q_{\text{out}}^k = \int_{\Gamma_o^k} \bar{\mathbf{u}} \cdot \mathbf{n} \, dS$ with $\mathbf{n}$ being the outward unit vector of Γ_o^k.

The reference pressure P_{ref} is set as a constant in this paper. It could also be specified by other models, for example, using the 3-element Windkessel model which considers the compliance of the downstream vessel [23,29]. More accurate physiologic behavior could be obtained by using a sophisticated model, however, there are also more empirical parameters need to be determined.

The resistance at the outlet R_{out}^k represents the pressure loss in the peripheral vasculature and induce flow distribution among the outlets. The resistance value at each outlet can be determined by distributing the total resistance R_{total} among the outlets. The total resistance was estimated from the mean blood pressure and the mean flow rate as

$$R_{\text{total}} = \frac{P_{\text{m}} - P_{\text{ref}}}{\bar{Q}_{\text{in}}}, \tag{11}$$

where $\bar{Q}_{\text{in}}$ is the mean flow rate and P_{m} is the mean blood pressure which is computed via $P_{\text{m}} = \frac{2}{3} P_d + \frac{1}{3} P_s$ where P_d is the diastolic pressure and P_s is the systolic pressure [30]. Correspondingly, the resistance of the individual outlet is given by

$$R_{\text{out}}^k = \frac{P_{\text{m}} - P_{\text{ref}}}{Q_{\text{out}}^k}, \quad k = 1, 2, \ldots, N_o. \tag{12}$$

Then, according to Murray's law [31], the flow rate has a relationship with the vessel size in the form of

$$Q \propto d^\gamma, \tag{13}$$

where d is the equivalent diameter of the vessel, γ is an empirical scaling exponent. For example, when Poiseuille's flow is considered, it is deduced that $\gamma = 3$. On the other hand, by considering the allometric laws relating flows to the volume of the tissue, it is obtained that $\gamma = 8/3$ [32]. In the same work, experimental observations shows that $\gamma > 8/3$.

(12) and (13) imply that the resistance of each branch is inversely related to the vessel size with the same morphometric exponent, thus $R_{\text{out}}^k \propto d_k^{-\gamma}$, where d_k is the equivalent diameter of the k-th outlet. Therefore, the total resistance R_{total} is distributed among outlets in the form that [18,30]

$$R_{\text{out}}^k = R_{\text{total}} \frac{1}{d_k^\gamma} \sum_{i=1}^{N_o} d_i^\gamma. \tag{14}$$

2.2. Finite element discretization

The LES problem described in (6) is discretized by an unstructured finite element method. Following the standard notations, we define the trial function space $\mathcal{V}$ for the velocity and the scalar function space $\mathcal{P}$ for the pressure as

$$\mathcal{V} = \{\mathbf{u} \in [H^1(\Omega)]^3 : \mathbf{u} = \mathbf{v}_I \text{ on } \Gamma_{\text{in}} \text{ and } \mathbf{u} = \mathbf{0} \text{ on } \Gamma_{\text{wall}}\}, \\ \mathcal{P} = L^2(\Omega) \tag{15}$$

and the weighting function space $\mathcal{V}_0$ for the velocity as:

$$\mathcal{V}_0 = \{\boldsymbol{\phi} \in [H^1(\Omega)]^3 : \boldsymbol{\phi} = \mathbf{0} \text{ on } \Gamma_{\text{in}} \cup \Gamma_{\text{wall}}\}. \tag{16}$$

Then, the weak form of the LES problem reads as: Find $\bar{\mathbf{u}} \in \mathcal{V}$ and $\bar{P} \in \mathcal{P}$, such that $\forall \boldsymbol{\phi} \in \mathcal{V}_0$ and $q \in \mathcal{P}$,

$$B_G(\{\bar{\mathbf{u}}, \bar{P}\}, \{\boldsymbol{\phi}, q\}) = 0, \tag{17}$$

with

$$\begin{aligned} B_G(\{\bar{\mathbf{u}}, \bar{P}\}, \{\boldsymbol{\phi}, q\}) = &\int_\Omega \frac{\partial \bar{\mathbf{u}}}{\partial t} \cdot \boldsymbol{\phi} d\Omega + \int_\Omega (\bar{\mathbf{u}} \cdot \nabla)\bar{\mathbf{u}} \cdot \boldsymbol{\phi} d\Omega - \int_\Omega \bar{P}(\nabla \cdot \boldsymbol{\phi}) d\Omega \\ &+ \int_\Omega 2\nu_t \mathbf{S}(\bar{\mathbf{u}}) : \mathbf{S}(\boldsymbol{\phi}) d\Omega + \int_{\Gamma_{\text{out}}} \mathbf{n} \cdot (\bar{P}\boldsymbol{\phi}) dS \\ &- \int_{\Gamma_{\text{out}}} \mathbf{n} \cdot [2\nu_t \mathbf{S}(\bar{\mathbf{u}}) \cdot \boldsymbol{\phi}] dS - \int_\Omega (\nabla \cdot \bar{\mathbf{u}}) q d\Omega. \end{aligned} \tag{18}$$

The first surface integral term in (18), which represents the contribution of the resistive boundary condition on the outlet Γ_{out}, can be modified by using (10) and rewritten as:

$$\begin{aligned} \int_{\Gamma_{\text{out}}} \mathbf{n} \cdot (\bar{P}\boldsymbol{\phi}) dS = &\sum_{k=0}^{N_o} \int_{\Gamma_{\text{out}}^k} \mathbf{n} \cdot (P_{\text{ref}}\boldsymbol{\phi}) dS \\ &+ \sum_{k=0}^{N_o} \int_{\Gamma_{\text{out}}^k} \mathbf{n} \cdot (R_{\text{out}}^k \int_{\Gamma_{\text{out}}^k} \bar{\mathbf{u}} \cdot \mathbf{n} dS) \boldsymbol{\phi} dS. \end{aligned} \tag{19}$$

The second term in (19) introduces an global connection among the variables on the outlet boundaries.

Then we discretize the weak form (17) in space with a $P_1 - P_1$ (linear velocity and linear pressure) finite element method. Because the $P_1 - P_1$ pair does not satisfy the Ladyzenskaya–Babuska–Brezzi (LBB) condition, additional stabilization terms are considered, such as the streamline upwind Petrov Galerkin method described in [33,34]. Denoting the finite element subspaces $\mathcal{V}^h$, $\mathcal{P}^h$ and $\mathcal{V}_0^h$ as the counterparts of their infinite dimensional subspaces, the semi-discretized system of the LES problem with the stabilization is described as: Find $\bar{\mathbf{u}}^h \in \mathcal{V}^h$ and $\bar{P}^h \in \mathcal{P}^h$, such that $\forall \boldsymbol{\phi}^h \in \mathcal{V}_0^h$ and $q^h \in \mathcal{P}^h$,

$$B(\{\bar{\mathbf{u}}^h, \bar{P}^h\}, \{\boldsymbol{\phi}^h, q^h\}) = 0, \tag{20}$$

with

$$B(\{\bar{u}^h, \bar{P}^h\}, \{\phi^h, q^h\})$$

$$= B_G(\{\bar{u}^h, \bar{P}^h\}, \{\phi^h, q^h\}) + \sum_{K \in \Omega_h} \left(\nabla \cdot \bar{u}^h, \ \tau_c \nabla \cdot \phi^h \right)_K$$

$$+ \sum_{K \in \Omega_h} \left(\frac{\partial \bar{u}^h}{\partial t} + \bar{u}^h \cdot \nabla \bar{u}^h + \nabla \bar{P}^h, \tau_m (\bar{u}^h \cdot \nabla \phi^h + \nabla q^h) \right)_K$$

$$+ \sum_{K \in \Omega_h} \left(\bar{U}^h \cdot \nabla \bar{u}^h, \phi^h \right)_K + \sum_{K \in \Omega_h} \left(\bar{U}^h \cdot \nabla \bar{u}^h, \tau_b (\bar{U}^h \cdot \nabla \phi^h) \right)_K$$

where $\Omega^h = \{K\}$ is the given unstructured tetrahedral mesh, $(\cdot, \cdot)_K$ represents an integral over the element K, $\bar{U}^h = \tau_m \left(\frac{\partial \bar{u}^h}{\partial t} + \bar{u}^h \cdot \nabla \bar{u}^h + \nabla \bar{P}^h \right)$ is the conservation-restoring advective velocity, and τ_m, τ_c and τ_b are the stabilization parameters defined as follows:

$$\tau_m = \frac{1}{\sqrt{4/(\Delta t)^2 + (\bar{u}^h \cdot G \cdot \bar{u}^h) + 36\nu_t^2 G : G}},$$

$$\tau_c = \frac{1}{8\tau_m \text{trace}(G)}, \quad (21)$$

$$\tau_b = \frac{1}{\sqrt{\bar{U}^h \cdot G \cdot \bar{U}^h}}.$$

Here $G_{ij} = \sum_{k=1}^{3} \frac{\partial \xi_k}{\partial x_i} \frac{\partial \xi_k}{\partial x_j}$ is the covariant metric tensor where $\frac{\partial \xi}{\partial x}$ represents the inverse Jacobian of the mapping between the reference and the physical domain, and Δt is the step size for the time discretization.

After the spatial discretization, we obtain a time-dependent semi-discretized nonlinear system

$$M \frac{du}{dt} + Nu + Qp + R = 0,$$
$$S \frac{du}{dt} + Q^T u + Kp = 0, \quad (22)$$

where u and p are the vectors of nodal values of the velocity and pressure functions, respectively, the entries of the matrices M, N, Q, S and K are defined as follows:

$$M_{ij} = \int_K \phi_j \cdot \phi_i \, d\Omega + \int_K \phi_j \cdot \left(\tau_m \bar{u} \cdot \nabla \phi_i \right) d\Omega,$$

$$N_{ij} = \int_K \left(\bar{u} \cdot \nabla \phi_j \right) \cdot \phi_i \, d\Omega + \int_K 2\nu_t S(\phi_j) : S(\phi_i) \, d\Omega$$

$$+ \int_K (\nabla \cdot \phi_j)(\tau_c \nabla \cdot \phi_i) \, d\Omega + \int_K \left(\bar{u} \cdot \nabla \phi_j \right) \cdot \left(\tau_m \bar{u} \cdot \nabla \phi_i \right) d\Omega$$

$$+ \int_K \left(\bar{U} \cdot \nabla \phi_j \right) \cdot \phi_i \, d\Omega + \int_K \left(\bar{U} \cdot \nabla \phi_j \right) \cdot \left(\tau_b \bar{u} \cdot \nabla \phi_i \right) d\Omega$$

$$Q_{ij} = -\int_K q_j (\nabla \cdot \phi_i) \, d\Omega + \int_K \nabla q_j \cdot \left(\tau_m \bar{u} \cdot \nabla \phi_i \right) d\Omega,$$

$$S_{ij} = \int_K \phi_j \cdot \nabla q_i \, d\Omega,$$

$$K_{ij} = \int_K \nabla q_j \cdot \tau_m \nabla q_i \, d\Omega,$$

and the vector R representing the contribution of the resistive boundary condition given by

$$R_i = \int_{\Gamma_{\text{out}}} n \cdot \left(P_{\text{ref}} \phi_i \right) dS$$

$$+ \sum_j u_j \sum_{k=0}^{N_o} \left(R_{\text{out}}^k \int_{\Gamma_{\text{out}}^k} \phi_j \cdot n \, dS \right) \left(\int_{\Gamma_{\text{out}}^k} n \cdot \phi_i \, dS \right)$$

$$- \sum_j u_j \int_{\Gamma_{\text{out}}} n \cdot \left[2\nu_t S(\phi_j) \cdot \phi_i \right] dS.$$

Here, ϕ_i and q_i are the basis functions on the i-th node of the mesh.

We then employ a second-order backward differentiation formula (BDF2) to discretize the semi-discrete system (22) in the time direction. That is, the time-dependent term in (22) is approximated by

$$\frac{du}{dt} = \frac{3u^n - 4u^{n-1} + u^{n-2}}{2\Delta t}, \quad \text{for } n \geq 2,$$

where u^n represent the value of u at the n-th time step, and Δt is the time step size. To provide an accurate approximation of u^1 in the above scheme, we separate the first time step into two fractional steps: (i) $(0, \frac{\Delta t}{2})$ and (ii) $(\frac{\Delta t}{2}, \Delta t)$, and employ a first-order backward Euler method for the first sub-time step and a BDF2 scheme for the second sub-time step.

The temporal discretization scheme is fully implicit. At each time step, we need to solve a sparse, nonlinear algebraic system to obtain the solution of the next time step. For simplicity of the following discussion, we rewrite the fully discretized system in the form:

$$\mathcal{F}(x) = 0, \quad (23)$$

where x represent the solution vector for both velocity u and pressure p at the n-th time step, and the superscript n is omitted for simplicity hereafter. For both the unknowns and the equations, a point-block ordering is used to organize the algebraic system on the mesh. The components of velocity and pressure are ordered node by node, and the approximate solution is defined as:

$$x = \left(u_0, v_0, w_0, p_0, u_1, v_1, w_1, p_1, \ldots, u_{M-1}, v_{M-1}, w_{M-1}, p_{M-1} \right)^T,$$

where M is the total number of mesh points. Similarly, the point-block ordering is used for $\mathcal{F}$. This ordering improves the robustness of ILU preconditioner, as well as the cache performance; see [35], for example.

2.3. Newton-Krylov-Schwarz algorithm

The fully discretized system (23) is usually very large in size. We use a parallel Newton–Krylov–Schwarz algorithm to solve it. Firstly, an inexact Newton method [36,37] is employed to solve the nonlinear system. At each Newton step, the new solution $x^{(k+1)}$ is obtained from the current approximate solution $x^{(k)}$ by adding the Newton correction $s^{(k)}$, such that

$$x^{(k+1)} = x^{(k)} + \theta^{(k)} s^{(k)}, \quad (24)$$

where $\theta^{(k)}$ is the step length calculated by the backtracking line-search [38], and the initial guess $x^{(0)}$ is given by the solution of the previous time step. The Newton correction $s^{(k)}$ is obtained by forming and solving the following right-preconditioned Jacobian system with a Krylov subspace method, such as GMRES [39],

$$J_k M_k^{-1} z^{(k)} = -\mathcal{F}(x^{(k)}), \quad z^{(k)} = M_k s^{(k)}. \quad (25)$$

Here, J_k is the Jacobian matrix evaluated at $x^{(k)}$, which we compute analytically by taking the first-order Fréchet derivative of the nonlinear system (22), and M_k^{-1} is the Schwarz preconditioner to be introduced shortly. The accuracy of the solution to the preconditioned Jacobian systems is controlled by a nonnegative relative tolerance η_k in the sense that

$$\|J_k s^{(k)} + \mathcal{F}(x^{(k)})\| \leq \eta_k \|\mathcal{F}(x^{(k)})\|.$$

If $\eta_k = 0$, then the algorithm reduces to the standard Newton method.

We next describe the construction of the preconditioner in (25) in detail. We employ a restricted additive Schwarz preconditioner [40] which is constructed as follows. First, we partition the computational domain Ω into n_p non-overlapping subdomains Ω_ℓ ($\ell = 1, \ldots, n_p$), where n_p is the same as the number of processors. To obtain a partition with good load balance, the package ParMETIS [41] is employed to decompose the mesh into parts with fairly equal number of unknowns. In addition, we insist that different outlets are assigned to different processor cores. Then, each subdomain is extended to an overlapping subdomain Ω_ℓ^δ by including δ layers of mesh elements from its adjacent subdomains. Here δ is an integer indicating the level of overlap.

On each overlapping subdomain Ω_ℓ^δ, we define the restriction operator R_ℓ^δ to be the matrix that maps the global vector of unknowns in Ω to those belonging to Ω_ℓ^δ, such that

$$x_\ell^\delta = R_\ell^\delta x = \left(I_\ell^\delta \quad 0 \right) \begin{pmatrix} x_\ell^\delta \\ x \backslash x_\ell^\delta \end{pmatrix},$$
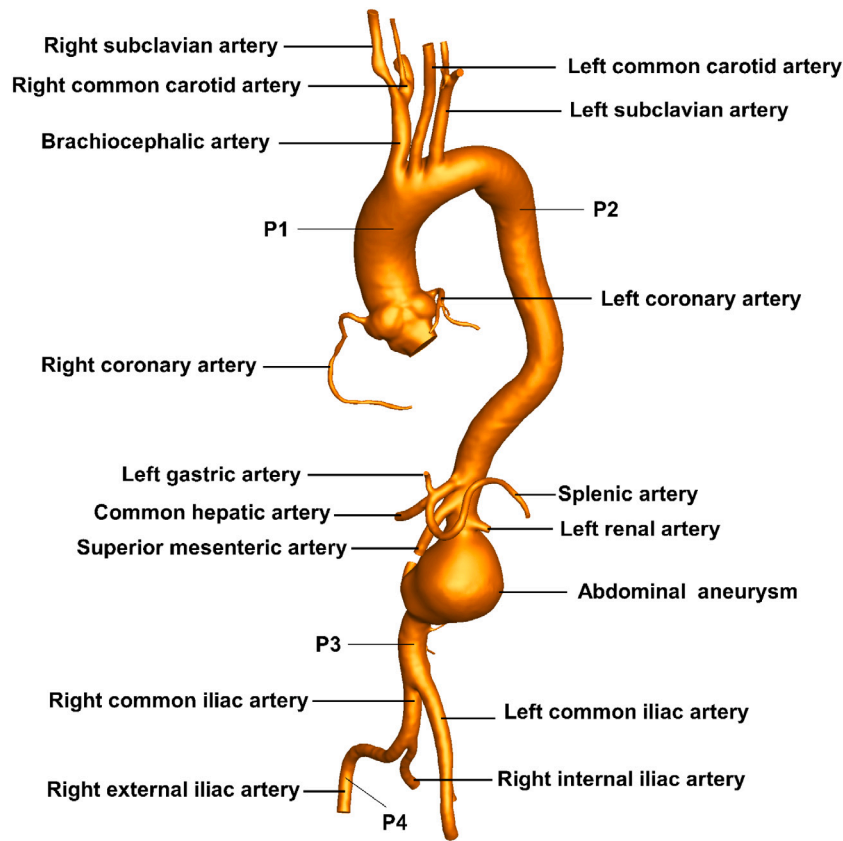
Fig. 1. A patient-specific aorta model. The four points P1–P4 are four positions we used for tracking the velocity and pressure.

where I_ℓ^δ is an identity matrix which has the same dimension as x_ℓ^δ, and $x\backslash x_\ell^\delta$ is a subvector denotes the unknowns outside the subdomain Ω_ℓ^δ. On the other hand, the transpose of the restriction, $(R_\ell^\delta)^T$, serves as a prolongation operator that maps a local vector defined on Ω_ℓ^δ to a global vector defined on the whole domain Ω by padding zeros in locations corresponding to $x\backslash x_\ell^\delta$. With the above definitions, we construct a subdomain Jacobian by

$$J_\ell^\delta = R_\ell^\delta J_k (R_\ell^\delta)^T, \quad \ell = 1, 2, \ldots, n_p,$$

which is the restriction of the global Jacobian matrix J_k to the subdomain Ω_ℓ^δ. Then, the restricted additive Schwarz preconditioner is defined as

$$M_k^{-1} = \sum_{\ell=1}^{n_p} (R_\ell^0)^T \left(\widetilde{J}_\ell^\delta \right)^{-1} R_\ell^\delta, \tag{26}$$

where R_ℓ^0 is the restriction operator to the unknowns in the non-overlapping subdomain Ω_ℓ, defined similarly as R_ℓ^δ, and $(\widetilde{J}_\ell^\delta)^{-1}$ is an approximate inverse matrix of the subdomain Jacobian J_ℓ^δ. In our application, the approximate inverse of the local subdomain Jacobian $(\widetilde{J}_\ell^\delta)^{-1}$ is obtained by using a point-block incomplete LU (ILU) factorization [42]. In the restricted additive Schwarz preconditioner, the prolongation operator of the overlapping subdomain is replaced by the corresponding non-overlapping one to reduce the communication cost when implemented on parallel computers.

3. Numerical results

In this section, we discuss some results obtained by applying the algorithm developed in the previous sections to a patient-specific aorta with an abdominal aneurysm. To determine a suitable mesh for the LES simulation, we first compare the LES results computed on two different meshes with a reference numerical solution obtained by direct numerical simulation (DNS) at high resolution. Then, we investigate the impacts of the parameters of the resistive boundary condition on the simulation results. Last, we present the convergence properties of the algorithm with various parameter settings, the robustness of the algorithm with respect to some physical and numerical parameters, and the parallel scalability of the algorithm.

The algorithm is implemented with the Portable Extensible Toolkit for Scientific computing (PETSc) library [43]. The numerical simulations are carried out on the Tianhe 2A supercomputer at the China National Supercomputer Center in Guangzhou. Each compute node has two 12-core Intel Ivy Bridge Xeon CPUs and 64 GB shared memory. In the following simulations, ILU with fill-in level 1 (ILU(1)) is used as the subdomain solver, the overlapping size of the subdomain is $\delta = 3$, and the relative tolerance for Newton and GMRES are 10^{-6} and 10^{-4}, respectively. These parameters are adopted through all the computations, unless otherwise specified.

3.1. Assessment of the computational meshes

We consider a patient-specific aorta consisting one inlet and 26 outlets, as shown in Fig. 1. The geometry is obtained from the segmentation of a contrast-enhanced CT image. At the inlet, we prescribe a pulsatile periodic flow wave with a period of 1.0 s, as shown in Fig. 2. The profile of the velocity on the inlet surface is assumed to be parabolic. The blood is characterized with a density of $1.06\,\mathrm{g/cm^3}$ and a kinematic viscosity of $0.035\,\mathrm{cm^2/s}$. The systolic Reynolds number is approximately 5300, which is based on the maximum inlet velocity and the equivalent vessel diameter of the inlet. The simulation is carried out with a time step size $\Delta t = 0.005$ s for two cardiac cycles. Numerical test shows that the third cycle of the pressure wave and outflow rates have the same pattern as the second cycle, which indicate that the simulation has reached a periodic steady state after one cycle. Therefore, we use the data in the second cycle for the following investigations. The
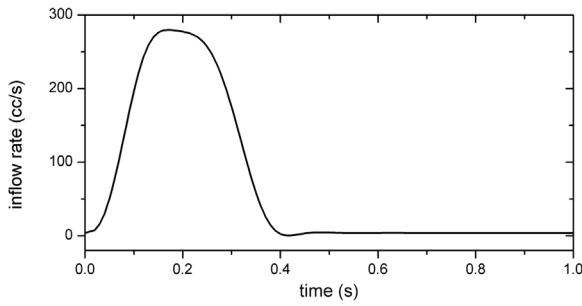
Fig. 2. The pulsatile flow rate profiles for one cardiac cycle.

Table 1
Information of the meshes used in the computations.

	No. of elements	No. of nodes	Mesh size (cm)	y^+
Mesh A	0.79 M	0.17 M	0.069	2.2
Mesh B	1.84 M	0.38 M	0.049	1.5
Mesh C	11.48 M	2.35 M	0.030	1.0

parameters for the resistive boundary conditions are set to be $P_{\text{ref}} = 0$ mmHg, $R_{\text{total}} = 500$ dyn s/cm^5, and $\gamma = 3$, respectively. For the LES, the constant of the σ-model is set as $C = 1.35$ [27].

The goal of LES is to obtain a reliable solution with a coarser mesh than the one needed to perform DNS, thus reduces the computational cost. To achieve this goal, the mesh for LES should be neither too fine, otherwise cannot reduce the computational cost, nor too coarse, such that the assumptions underlying the LES model remain valid. In the context of hemodynamics we are considering, we cannot refer to a statistically homogeneous isotropic and stationary turbulent regime; hence, the classical Kolmogorov theory cannot be used to determine a suitable mesh size for LES. For this reason, alternatively, we try to find a suitable mesh size for the LES by comparing the LES results to a reference numerical solution obtained by DNS at high resolution. Three finite element meshes are used in our simulations, as listed in Table 1. Here, as usual, the mesh size in the bulk is defined as the mean cubic root of the volume of the element, the mesh adjacent to the wall is characterized by the dimensionless wall distance y^+ which is defined as $y^+ \equiv u^* y/\nu$, where ν is the kinematic viscosity of the fluid, y is the size of the mesh adjacent to the wall, and $u^* = \sqrt{\tau_w/\rho}$ is the friction velocity at the wall. Here, τ_w is the wall shear stress given by

$$\tau_w = \sigma \cdot n - (n \cdot \sigma \cdot n)n, \qquad (27)$$

with $\sigma = -\bar{P}I + 2\nu S$ being the Cauchy stress tensor and n being the unit outward normal vector on the wall. The finest Mesh C is used for the DNS to obtain the reference solution, and Mesh A and B are used for the LES computations.

In LES, the subgrid scale stress accounts for the effect of the unresolved scale. The major role of the unresolved scale is to dissipate the energy transfer from the motion of large scales. To assess the turbulence model and the effect of the mesh size, we make a comparison of the energy dissipation rate. Fig. 3 shows the time history of the energy dissipation rate due to the viscosity

$$\varepsilon_v = \int_\Omega 2\nu S(\bar{u}) : S(\bar{u}) d\Omega,$$

and the energy dissipation rate due to the subgrid-scale stress

$$\varepsilon_{\text{sgs}} = \int_\Omega 2\nu_{\text{sgs}} S(\bar{u}) : S(\bar{u}) d\Omega.$$

Then we compare the total dissipation rate $\varepsilon_t = \varepsilon_v + \varepsilon_{\text{sgs}}$ with the result of the reference solution ε_{ref} obtained by DNS. Because a finer mesh usually leads to a larger velocity gradient, we could see that the viscosity dissipation of mesh B is larger than that of mesh A. It could also be observed that the SGS dissipation provides a good supplement to

the viscosity dissipation, since in both calculations with mesh A and B, the total dissipation rates are very consistent with the reference result. This confirms the good performance of the σ-model.

Next, we compare some LES results of Mesh A and B with the reference solution. Fig. 4 shows the time history of the computed pressure at 4 different positions marked with P1–P4 in Fig. 1. Both LES results are very close to the reference solution except at P4 where the LES result is slightly smaller than the reference result during the systole phase. Fig. 5 shows the computed flow rate for four branches, namely the right coronary artery, the common carotid artery, the common hepatic artery and the right internal iliac artery. The LES results also agree well with the reference result.

Figs. 6 and 7 further compare the velocity distribution in the cross section of the abdominal aneurysm at the early systole phase $t = 1.2$ s and in the mid-systole phase $t = 1.3$ s, respectively. We can see that the major velocity pattern in LES and DNS are very similar, while the flow details of LES with the fine mesh B is closer to the reference result.

Finally, Fig. 8 shows the magnitude of the wall shear stress (WSS) at the systole phase $t = 1.2$ s. We can see that the pattens of the WSS distribution of the LES are similar to the reference solution, while the WSS magnitude of LES is a little smaller than the reference solution in some areas, especially for the result of Mesh A. The peak of the WSS magnitude of the reference solution is 197.2, while they are 135.6 and 189.4 for the LES of Mesh A and B, respectively. The spatially averaged wall shear stress of the reference solution is 15.9, while they are 11.5 and 13.7 for the LES of Mesh A and B, respectively. Here, the spatially averaged wall shear stress is obtained by integrating the WSS on the entire wall surface of the arteries and then normalized over the area, that is,

$$SAWSS = \frac{1}{A} \int_{\Gamma_{\text{wall}}} \tau_w \, dA,$$

where A is the total area of the wall surface of the whole arteries. In terms of the wall shear stress, the LES result of Mesh B is much better than that of Mesh A. Therefore, for the rest of the paper, we use Mesh B for the LES computations.

3.2. Impact of the parameters of the resistive boundary condition

There are three parameters for the resistive boundary condition, the reference pressure P_{ref}, the total resistance R_{total} and the scaling exponent γ. In this section, we investigate the impact of these parameters on the simulation results. For the purpose of comparison, we calculate the pressure at four different positions P1–P4, the outflow rates at four branches A1–A4, the spatially averaged wall shear stress and the peak wall shear stress. Here, P1–P4 are the positions marked in Fig. 1, and A1–A4 stand for the right coronary artery, the common carotid artery, the common hepatic artery and the right internal iliac artery, respectively, as the same in Fig. 5. The comparison results at the systole phase $t = 1.2$ s with different parameters are summarized in Tables 2–4.

Table 2 shows the impact of the reference pressure on the flow rate, the pressure and the wall shear stress. We could see that the flow rates at the outlet branches and the wall shear stress are not affected at all by the change of the reference pressure, they stay at the same values when P_{ref} goes from 0 to 20 mmHg. Only the pressure field is influenced by the change of the reference pressure. It is observed that the pressure at these four positions increases by the same amount compared to the reference pressure. This is in line with the theory for the incompressible flow that it is the pressure variation not the pressure base state affects the flow.

Table 3 shows the impact of the total resistance. We see that the pressure at all the four positions increase significantly with the increase of the total resistance. Moreover, the pressure is influenced in a different way comparing with the reference pressure in Table 2. Here the distribution of the pressure is changed for different total resistance. The flow rates and the wall shear stress are affected not
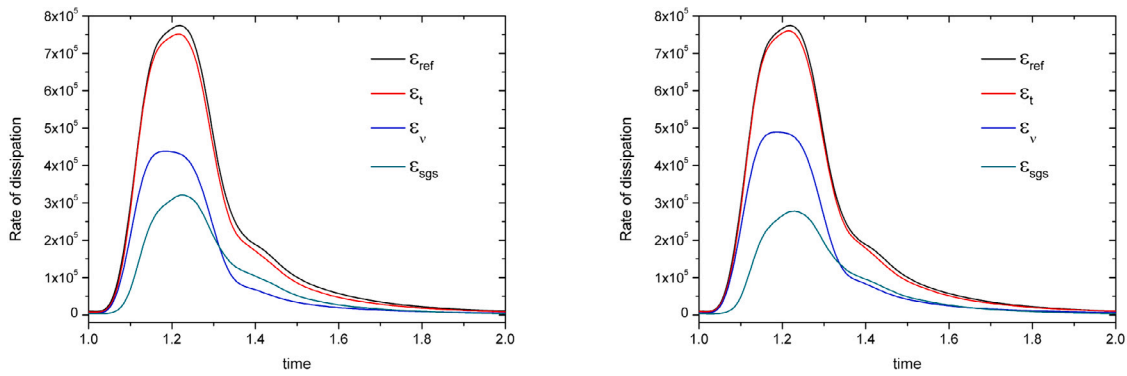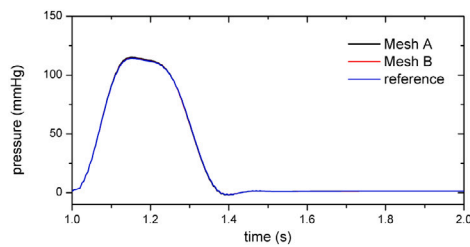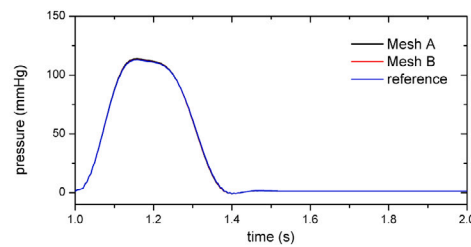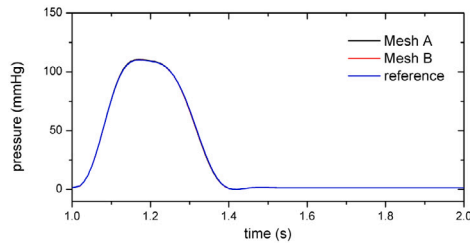
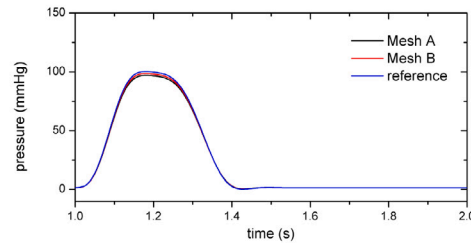**Fig. 3.** The time history of the dissipation rate. Left: Mesh A; right: Mesh B.

(a) P1 in the ascending aorta

(b) P2 in the thoracic aorta

(c) P3 in the abdominal aorta

(d) P4 in the right external iliac artery

Fig. 4. The time history of pressure at four different positions.

so greatly as the pressure. As the total resistance increases, the flow rate at A4 increases slightly while they decrease slightly at A1–A3, and both the averaged and peak wall shear stress increase slightly. The equivalent vessel diameters for A1–A4 are 0.16, 0.66, 0.60 and 0.84 cm, respectively. It means that a higher total resistance would enhance the flow rates at the larger outlet branches and decrease the flow rate at the smaller branches.

Table 4 shows the impact of the scaling exponent. We see that as the scaling exponent increases, the pressure increase slightly at P1–P3 and decreases slightly at P4, the flow rates decrease dramatically at A1–A3 and increases markedly at A4 (the largest outlet), the spatially averaged wall shear stress decrease mildly, while the peak wall shear stress decrease greatly. Overall, the flow field is influenced markedly by the change of the scaling exponent, while the pressure field is not much affected.

3.3. Convergence performance with respect to the overlapping size and subdomain solver

In this section, we study the impact of the size of subdomain overlap and the subdomain solver, which play an critical role in the overall algorithm performance. We investigate the performance of the

Table 2
Impact of the reference pressure on the simulation results.

P_{ref} (mmHg)		0	10	20
Pressure (mmHg)	P1	111.8	121.8	131.8
	P2	111.0	121.0	131.0
	P3	109.1	119.1	129.1
	P4	99.9	109.9	119.9
Flow rate (cc/s)	A1	0.29	0.29	0.29
	A2	20.16	20.16	20.16
	A3	14.99	14.99	14.99
	A4	39.76	39.76	39.76
Wall shear stress (dyn/cm^2)	$|\tau_w|_{max}$	189.4	189.4	189.4
	$|\tau_w|_{mean}$	13.7	13.7	13.7

algorithm with respect to different overlapping size, and for each case, ILU with different fill-in levels are applied as the subdomain solver. The detailed results of the numbers of Newton and GMRES iterations together with the averaged computing time per Newton step are shown in Table 5. Here, incomplete LU with fill-in level k is denoted as ILU(k), and ILU(0), ILU(1), and ILU(2) are tested. For all the test cases, the number of Newton iterations is insensitive to the subdomain solver. The averaged number of GMRES iterations per Newton step decreases
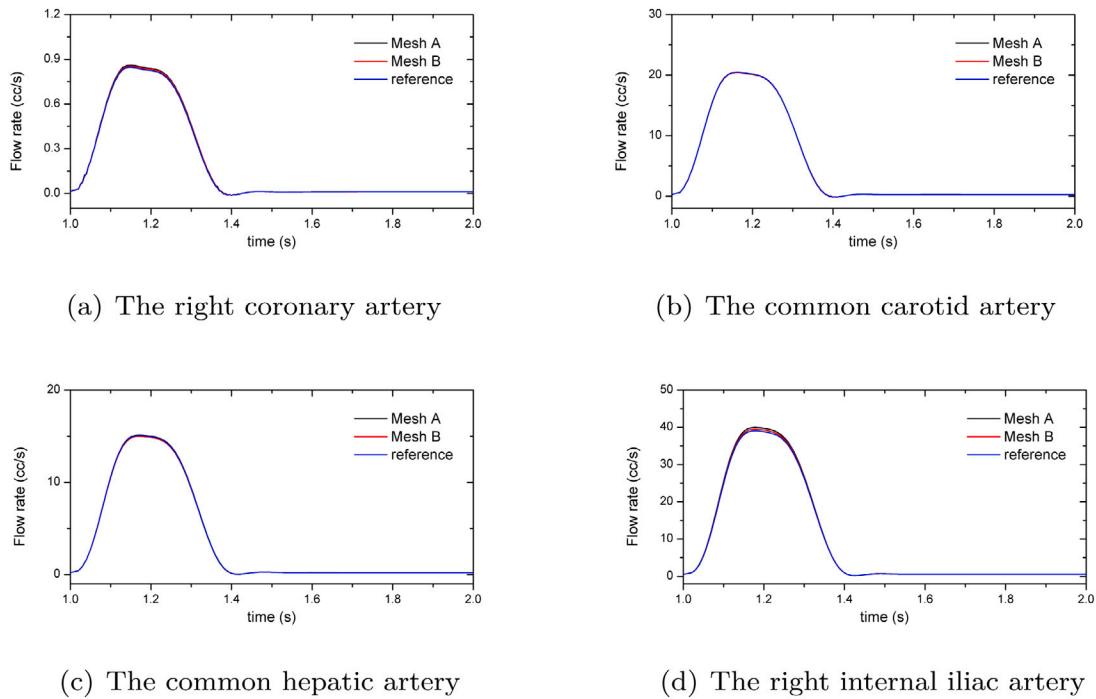
(a) The right coronary artery

(b) The common carotid artery

(c) The common hepatic artery

(d) The right internal iliac artery

Fig. 5. The time history of flow rates at four different arteries.

(a) Mesh A

(b) Mesh B

(c) Reference result

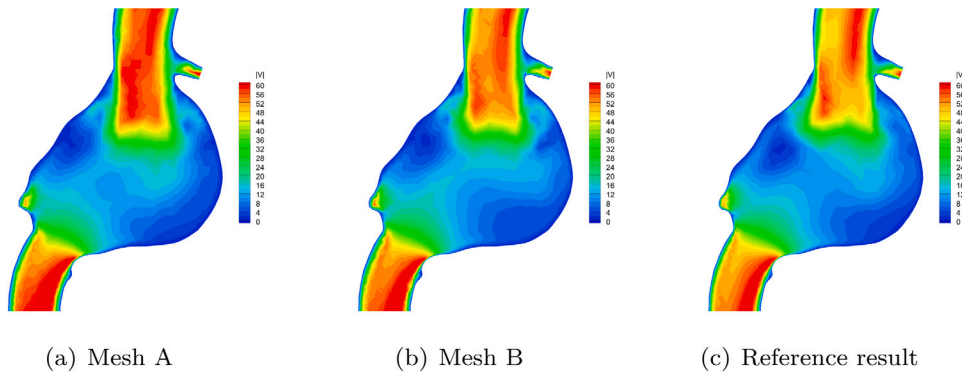**Fig. 6.** The velocity distribution in the cross section of the abdominal aneurysm at the early systole phase $t = 1.2$ s.

(a) Mesh A

(b) Mesh B
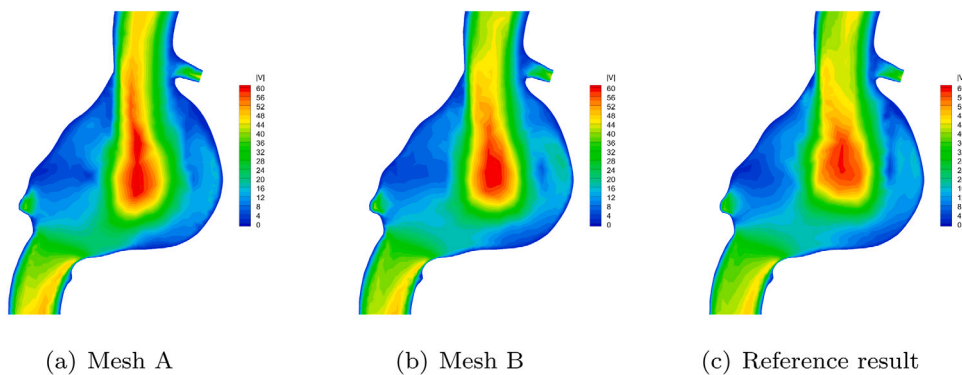

(c) Reference result

Fig. 7. The velocity distribution in the cross section of the abdominal aneurysm in the mid-systole phase $t = 1.3$ s.

dramatically as the level of fill-ins increases, especially from ILU(0) to ILU(1). However, the computing time decreases not that much with the increase of fill-ins. ILU(1) only reduces the computing time by a little compared with ILU(0), and ILU(2) does not decrease the computing time further, because its cost per iteration is higher than ILU(1) and the

reduction of the number of GMRES iterations cannot compensate for the extra cost such as construction of the preconditioner. For each case of δ, ILU(1) always provides the best result. On the other hand, when using the same subdomain solver, we could see a larger overlap improves the linear solver convergence in terms of the GMRES iterations
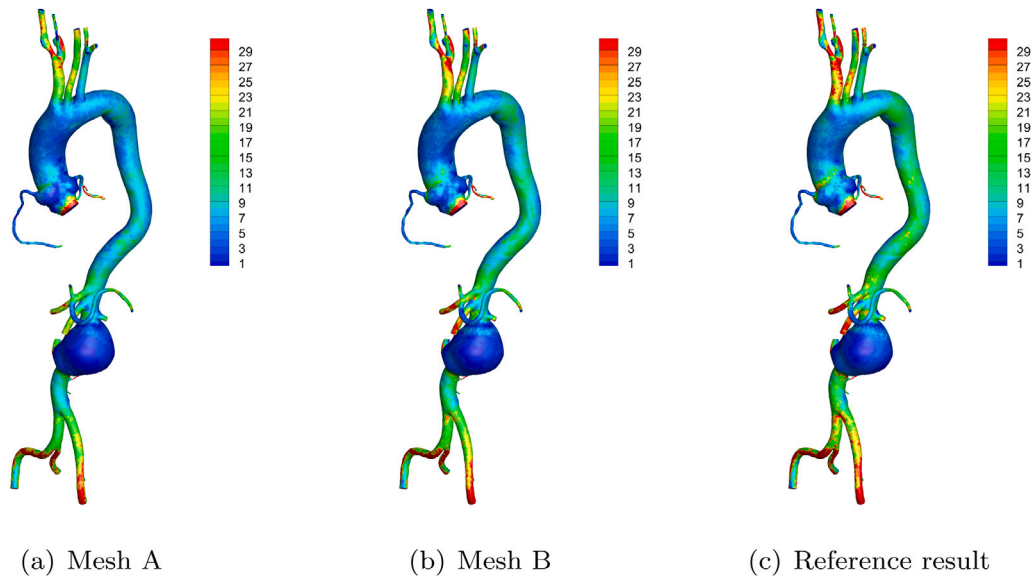
(a) Mesh A (b) Mesh B (c) Reference result

Fig. 8. The spatial distribution of the wall shear stress at the early systole phase $t = 1.2\,\text{s}$.

Table 3
Impact of the total resistance on the simulation results.

R_{total}		400	500	600
Pressure (mmHg)	P1	91.0	111.8	132.6
	P2	90.2	111.0	131.9
	P3	88.3	109.1	129.9
	P4	79.2	99.9	120.5
Flow rate (cc/s)	A1	0.30	0.29	0.29
	A2	20.32	20.16	20.04
	A3	15.07	14.99	14.93
	A4	39.61	39.76	39.85
Wall shear stress (dyn/cm^2)	$|\tau_w|_{\max}$	189.1	189.4	189.6
	$|\tau_w|_{\text{mean}}$	13.7	13.7	13.7

Table 4
Impact of the scaling exponent of the resistance on the simulation results.

γ		8/3	3	4
Pressure (mmHg)	P1	111.3	111.8	114.0
	P2	110.5	111.0	113.3
	P3	108.7	109.1	111.0
	P4	100.5	99.9	98.8
Flow rate (cc/s)	A1	0.47	0.29	0.07
	A2	20.30	20.16	19.00
	A3	15.54	14.99	12.91
	A4	37.26	39.76	46.42
Wall shear stress (dyn/cm^2)	$|\tau_w|_{\max}$	296.6	189.4	114.5
	$|\tau_w|_{\text{mean}}$	13.9	13.7	13.4

Table 5
Performance of the algorithm with respect to different size of subdomain overlap and different subdomain solver.

δ	Subsolver	Newton	GMRES	Time
1	ILU(0)	2.83	716.1	96.75
	ILU(1)	2.83	389.8	82.57
	ILU(2)	2.83	299.2	98.80
2	ILU(0)	2.83	679.4	91.86
	ILU(1)	2.83	373.5	79.63
	ILU(2)	2.83	223.3	83.86
3	ILU(0)	2.83	657.0	90.76
	ILU(1)	2.83	307.3	73.29
	ILU(2)	2.83	237.8	87.05
4	ILU(0)	2.83	638.0	86.40
	ILU(1)	2.83	314.2	73.74
	ILU(2)	2.83	220.5	85.73

Table 6. Here, $\Delta t = 0.005\,\text{s}$, $P_{\text{ref}} = 0$ mmHg, $R_{\text{total}} = 500\ \text{dyn} \cdot \text{s/cm}^5$, $\gamma = 3$ and $\nu = 0.016\ \text{cm}^2/\text{s}$ are applied, except when they are changed for the robustness study.

Firstly, we investigate the impact of the time step size. Since we use a fully implicit scheme in the time discretization, it usually allows us to use a large time step size in the simulation. Table 6 shows how the time step size influence the convergence of the algorithm. We see that the numbers of Newton and GMRES iterations together with the computing time both increase gently as Δt increases from 0.0025 to 0.01, then they increase rapidly when Δt further increases to 0.02. For practical applications, since time accurate solutions are needed, the time step size is often much smaller than 0.01.

Next, we investigate how the parameters of the resistive boundary condition influence the performance of the algorithm. Table 6 shows that the change of reference pressure P_{ref} and the scaling exponent γ does not affect the convergence of the algorithm markedly. We could also see that as the total resistance R_{total} increases, the number of Newton iterations stays as a constant, while there is a little increase for the number of GMRES iterations and the computing time. Overall, the convergence of the algorithm is not sensitive to the parameters of the resistive boundary condition.

We then investigate the impact of the viscosity. The viscosity is an important physical parameter for blood flows. A smaller viscosity value often corresponds to a more complicated flow pattern, and at the

because it has more information from its neighbors. However, the cost per iteration for communication and computation also increases with a larger overlapping size. It is always a trade off to choose the parameter δ. The best choice is $\delta = 3$ for ILU(0) and ILU(1), and $\delta = 2$ for ILU(2). Based on the above results, we take the optimal choice of overlapping size $\delta = 3$ and subdomain solver ILU(1) for all test cases throughout the rest of the paper.

3.4. Robustness and scalability

We next study the robustness and the parallel scalability of the proposed algorithm. We consider the robustness of the algorithm with respect to the time step size, the parameters of the resistive boundary condition, and the viscosity of the fluid. The results are summarized in

Table 6
The robustness of the algorithm with respect to the time step size, the parameters of the resistive boundary condition, and the viscosity of the fluid.

		Newton	GMRES	Time
Δt (s)	0.0025	2.17	280.8	55.47
	0.005	2.83	307.3	73.29
	0.01	3.00	422.5	92.57
	0.02	4.66	636.5	227.1
P_{ref} (mmHg)	0	2.83	307.3	73.29
	10	2.83	315.1	73.76
	20	2.83	315.1	73.88
R_{total} (dyn s/cm^5)	400	2.83	289.8	69.42
	500	2.83	307.3	73.29
	600	2.83	348.4	78.47
γ	8/3	2.83	331.0	74.12
	3	2.83	307.3	73.29
	4	2.83	326.8	75.84
ν (cm^2/s)	0.025	2.83	344.2	79.96
	0.030	2.83	338.8	78.42
	0.035	2.83	307.3	73.29
	0.045	2.83	302.7	72.87
	0.055	2.83	291.0	69.60

Table 7
Parallel performance of the proposed algorithm. The subdomain overlapping size is $\delta = 3$, and ILU(1) is used as the subdomain solver.

n_p	Newton	GMRES	Time	Speedup	Ideal	Efficiency
128	2.83	307.3	72.73	1	1	100%
256	2.83	322.8	45.56	1.81	1	91%
512	2.83	375.1	23.01	3.16	2	79%
1024	2.83	373.8	13.32	5.46	4	68%

same time, the corresponding nonlinear/linear systems become harder to solve since the Jacobian matrix is less diagonally dominant. From Table 6, we observe that the number of Newton iterations does not change as the viscosity becomes smaller, while the number of GMRES iterations increases slightly for smaller viscosities, and as a result the computing time also increases slightly. All cases converge well, which implies that the algorithm is robust with respect to the viscosity of the fluid.

Finally, we investigate the parallel scalability of the algorithm. As shown in Table 7, as the number of processor cores increases, the number of Newton iterations stays at a constant while the number of GMRES iterations grows mildly. The overall speedup from 128 to 1024 cores is around 5.46 and the corresponding parallel efficiency is 68%, which shows that the proposed algorithm has a good parallel scalability.

4. Concluding remarks

We developed a fully-implicit finite element method and a parallel domain decomposition algorithm for the large eddy simulation of blood flows in human arteries. Resistive boundary conditions are applied to the outlet boundaries of the arterial network. The σ-model based on the singular values of the stress tensor is applied to model the subgrid-scale stresses, and then the system of the LES equations is discretized using a stabilized finite element method in space and an second-order fully implicit BDF scheme in time. The resulting nonlinear system is solved using an inexact Newton method, where the Jacobian system is solved using a Krylov subspace method together with a Schwarz preconditioner with analytical Jacobian. Due to the coupling of resistive boundary condition, the Jacobian matrix has a dense block corresponding to all the variables on the outlet boundary. We tested the algorithm using a patient-specific case of human aorta with 26 outlets. The accuracy and applicability of the proposed method are validated by comparing the LES results with a reference DNS solution. The performance of the proposed method is tuned by changing the

subdomain solver and the overlapping size. Results of numerical experiments show that the algorithm is stable with large time step size and is robust with respect to the physical and numerical parameters, and is scalable on a supercomputer with more than 1000 processor cores. Using this technology, the simulation of unsteady blood flows in a full three-dimensional, patient-specific arterial tree can be obtained in less than a few hours. In order to apply the techniques for clinical applications, more works are needed, such as realistic input parameters for the boundary conditions. It is important to note that the accuracy of blood flow simulations is critically dependent on the appropriate setting of boundary conditions. However, high-fidelity boundary condition for patient-specific hemodynamic simulations is still a challenging problem since it is difficult to obtain all the flow information at the boundaries, especially for the arterial network with many branches. Therefore, reliable boundary conditions for clinical applications by incorporating the patient-specific physiological data will be an important subject of future developments.

CRediT authorship contribution statement

Zi-Ju Liao: Methodology, Software, Writing – original draft. **Shanlin Qin:** Resources, Investigation. **Rongliang Chen:** Software, Validation. **Xiao-Chuan Cai:** Conceptualization, Supervision.

Declaration of competing interest

Acknowledgments

References

[1] Geers AJ, Larrabide I, Morales HG, Frangi AF. Approximating hemodynamics of cerebral aneurysms with steady flow simulations. J Biomech 2014;47(1):178–85.

[2] Vergara C, Le Van D, Quadrio M, Formaggia L, Domanin M. Large eddy simulations of blood dynamics in abdominal aortic aneurysms. Med Eng Phys 2017;47:38–46.

[3] Taylor CA, Fonte TA, Min JK. Computational fluid dynamics applied to cardiac computed tomography for noninvasive quantification of fractional flow reserve: scientific basis. J Am Coll Cardiol 2013;61(22):2233–41.

[4] Blanco PJ, Bulant CA, Müller LO, Talou GM, Bezerra CG, Lemos PL, Feijóo RA. Comparison of 1D and 3D models for the estimation of fractional flow reserve. Sci Rep 2018;8(1):17275.

[5] Kakalis NMP, Mitsos AP, Byrne JV, Ventikos Y. The haemodynamics of endovascular aneurysm treatment: a computational modelling approach for estimating the influence of multiple coil deployment. IEEE Trans Med Imaging 2008;27(6):814–24.

[6] Cebral JR, Mut F, Raschi M, Scrivano E, Ceratto R, Lylyk P, Putman CM. Aneurysm rupture following treatment with flow-diverting stents: computational hemodynamics analysis of treatment. American Journal of Neuroradiology 2011;32(1):27–33.

[7] Gallo D, Lefieux A, Morganti S, Veneziani A, Reali A, Auricchio F, Conti M, Morbiducci U. A patient-specific follow up study of the impact of thoracic endovascular repair (TEVAR) on aortic anatomy and on post-operative hemodynamics. Comput & Fluids 2016;141:54–61.

[8] Morris PD, Narracott A, von Tengg-Kobligk H, Soto DAS, Hsiao S, Lungu A, Evans P, Bressloff NW, Lawford PV, Hose DR, et al. Computational fluid dynamics modelling in cardiovascular medicine. Heart 2016;102(1):18–28.

[9] Dolan JM, Kolega J, Meng H. High wall shear stress and spatial gradients in vascular pathology: a review. Ann Biomed Eng 2013;41(7):1411–27.

[10] Piccinelli M, Vergara C, Antiga L, Forzenigo L, Biondetti P, Domanin M. Impact of hemodynamics on lumen boundary displacements in abdominal aortic aneurysms by means of dynamic computed tomography and computational fluid dynamics. Biomech Model Mechanobiol 2013;12(6):1263–76.

[11] Marzo A, Singh P, Reymond P, Stergiopulos N, Patel U, Hose R. Influence of inlet boundary conditions on the local haemodynamics of intracranial aneurysms. Comput Methods Biomech Biomed Eng 2009;12(4):431–44.

[12] Madhavan S, Kemmerling EMC. The effect of inlet and outlet boundary conditions in image-based CFD modeling of aortic flow. Biomed Eng Online 2018;17(1):1–20.

[13] Pereira VM, Brina O, Gonzales AM, Narata AP, Bijlenga P, Schaller K, Lovblad KO, Ouared R. Evaluation of the influence of inlet boundary conditions on computational fluid dynamics for intracranial aneurysms: a virtual experiment. J Biomech 2013;46(9):1531–9.

[14] Piskin S, Celebi MS. Analysis of the effects of different pulsatile inlet profiles on the hemodynamical properties of blood flow in patient specific carotid artery with stenosis. Comput Biol Med 2013;43(6):717–28.

[15] Campbell IC, Ries J, Dhawan SS, Quyyumi AA, Taylor WR, Oshinski JN. Effect of inlet velocity profiles on patient-specific computational fluid dynamics simulations of the carotid bifurcation. J Biomech Eng 2012;134(5).

[16] Grinberg L, Karniadakis GE. Outflow boundary conditions for arterial networks with multiple outlets. Ann Biomed Eng 2008;36(9):1496–514.

[17] Lancellotti RM, Vergara C, Valdettaro L, Bose S, Quarteroni A. Large eddy simulations for blood dynamics in realistic stenotic carotids. Int J Numer Methods Biomed Eng 2017;33(11):e2868.

[18] Bulant CA, Blanco PJ, Talou GDM, Bezerra CG, Lemos PA, Feijóo RA. A head-to-head comparison between CT- and IVUS-derived coronary blood flow models. J Biomech 2017;51:65–76.

[19] Kim HJ, Figueroa CA, Hughes TJR, Jansen KE, Taylor CA. Augmented Lagrangian method for constraining the shape of velocity profiles at outlet boundaries for three-dimensional finite element simulations of blood flow. Comput Methods Appl Mech Engrg 2009;198(45–46):3551–66.

[20] Moghadam ME, Bazilevs Y, Hsia T-Y, Vignon-Clementel IE, Marsden AL, et al. A comparison of outlet boundary treatments for prevention of backflow divergence with relevance to blood flow simulations. Comput Mech 2011;48(3):277–91.

[21] Xu H, Baroli D, Di Massimo F, Quaini A, Veneziani A. Backflow stabilization by deconvolution-based large eddy simulation modeling. J Comput Phys 2020;404:109103.

[22] Vignon-Clementel IE, Figueroa CA, Jansen KE, Taylor CA. Outflow boundary conditions for three-dimensional finite element modeling of blood flow and pressure in arteries. Comput Methods Appl Mech Engrg 2006;195(29–32):3776–96.

[23] Vignon-Clementel IE, Figueroa C, Jansen K, Taylor C. Outflow boundary conditions for 3D simulations of non-periodic blood flow and pressure fields in deformable arteries. Comput Methods Biomech Biomed Eng 2010;13(5):625–40.

[24] Wu Y, Cai X-C. A parallel two-level method for simulating blood flows in branching arteries with the resistive boundary condition. Comput & Fluids 2011;45(1):92–102.

[25] Wu Y, Cai X-C. A parallel domain decomposition algorithm for simulating blood flow with incompressible Navier-Stokes equations with resistive boundary condition. Commun Comput Phys 2012;11(4):1279–99.

[26] Ku DN. Blood flow in arteries. Annu Rev Fluid Mech 1997;29(1):399–434.

[27] Nicoud F, Toda HB, Cabrit O, Bose S, Lee J. Using singular values to build a subgrid-scale model for large eddy simulations. Phys Fluids 2011;23(8):085106.

[28] Formaggia L, Quarteroni A, Veneziani A. Cardiovascular Mathematics: Modeling and Simulation of the Circulatory System. Berlin, Germany: Springer Science & Business Media; 2010.

[29] Nguyen MT, Jeon BJ, Chang H-J, Lee S-W. Domain decomposition based parallel computing for multi-scale coronary blood flow simulations. Comput & Fluids 2019;191:104254.

[30] Fossan FE, Sturdy J, Müller LO, Strand A, Bråten AT, Jørgensen A, Wiseth R, Hellevik LR. Uncertainty quantification and sensitivity analysis for computational FFR estimation in stable coronary artery disease. Cardiovasc Eng Technol 2018;9(4):597–622.

[31] Murray CD. The physiological principle of minimum work: I. The vascular system and the cost of blood volume. Proc Natl Acad Sci 1926;12(3):207–14.

[32] West GB, Brown JH, Enquist BJ. A general model for the origin of allometric scaling laws in biology. Science 1997;276(5309):122–6.

[33] Taylor CA, Hughes TJR, Zarins CK. Finite element modeling of blood flow in arteries. Comput Methods Appl Mech Engrg 1998;158(158):155–96.

[34] Whiting CH, Jansen KE. A stabilized finite element method for the incompressible Navier-Stokes equations using a hierarchical basis. Internat J Numer Methods Fluids 2001;35(1):93–116.

[35] Gropp WD, Kaushik DK, Keyes DE, Smith BF. High-performance parallel implicit CFD. Parallel Comput 2001;27(4):337–62.

[36] Eisenstat SC, Walker HF. Globally convergent inexact Newton methods. SIAM J Optim 1994;4(2):393–422.

[37] Eisenstat SC, Walker HF. Choosing the forcing terms in an inexact Newton method. SIAM J Sci Comput 1996;17(1):16–32.

[38] Nocedal J, Wright SJ. Numerical Optimization. New York: Springer Science & Business Media; 2006.

[39] Saad Y, Schultz MH. GMRES: A generalized minimal residual algorithm for solving nonsymmetric linear systems. SIAM J Sci Stat Comput 1986;7(3):856–69.

[40] Cai X-C, Sarkis M. A restricted additive Schwarz preconditioner for general sparse linear systems. SIAM J Sci Comput 1999;21(2):792–7.

[41] Karypis G, Aggarwal R, Schloegel K, Kumar V, Shekhar S. METIS/ParMETIS web page, University of Minnesota. 2013, http://glaros.dtc.umn.edu/gkhome/views/metis/.

[42] Saad Y. Iterative Methods for Sparse Linear Systems. Philadelphia: SIAM; 2003.

[43] Balay S, Abhyankar S, Adams M, Brown J, Brune P, Buschelman K, Dalcin L, Eijkhout V, Gropp W, Kaushik D, Knepley M, McInnes L, Rupp K, Smith B, Zampini S, Zhang H. PETSc users manual. Argonne National Laboratory; 2020.